IEEE Access
Multidisciplinary ⋮ Rapid Review ⋮ Open Access Journal

Received 31 March 2026, accepted 24 April 2026, date of publication 12 May 2026, date of current version 19 May 2026.
Digital Object Identifier 10.1109/ACCESS.2026.3692396

RESEARCH ARTICLE

Full-Wave Characterization of Reverberation Chambers for Rodent Bioassays: Methodology and Realistic-Loading Impact Analysis

ANTONIO FARAONE[1], (Senior Member, IEEE), GIORGI BIT-BABIK[1], (Senior Member, IEEE), KEVIN SANDERSON[2], PAOLA RUSSO[3], (Senior Member, IEEE), ALFREDO DE LEO[3], (Senior Member, IEEE), VALTER MARIANI PRIMIANI[3], (Senior Member, IEEE), AND VALERIO DE SANTIS[4], (Senior Member, IEEE)
[1]Motorola Solutions Inc., Fort Lauderdale, FL 33301, USA
[2]University of Illinois Urbana–Champaign, Champaign, IL 61801, USA
[3]Università Politecnica delle Marche, 60131 Ancona, Italy
[4]Università degli Studi dell'Aquila, 67100 L'Aquila, Italy

Corresponding author: Antonio Faraone (antonio.faraone@ieee.org)

ABSTRACT This study presents a comprehensive full-wave numerical dosimetry approach for large-scale rodent bioassays in Reverberation Chambers (RCs), improving upon prior methods that rely on idealized Plane Wave (PW) superposition. A "digital twin" of the Università Politecnica delle Marche RC was implemented using Transmission-Line Matrix and Finite Element Method solvers to characterize exposure homogeneity across rodent cages at 900 MHz. Unlike PW-superposition models, loaded-RC simulations account for realistic experimental constraints, such as intruding water-supply metal piping, specific antenna designs and placements, and actual mode stirrers. The loaded-RC electromagnetic characteristics were investigated by analyzing the field impedance ratios, yielding discrimination criteria for the probe location and type. Cage-wise instantaneous and ensemble-averaged whole-body specific absorption rate (wbSAR) distributions were evaluated using postured homogeneous rat models. Furthermore, investigations into exposure imbalance mitigation strategies demonstrated significant benefits when spinning cage assemblies. An analysis of mass-dependent exposures revealed a notably weaker correlation between body mass and wbSAR, as well as a much larger wbSAR cage dependence, compared to earlier PW-based predictions, further highlighting the necessity of realistic RC modeling for reliable rodent bioassay exposure design.

INDEX TERMS Radio-frequency dosimetry, specific absorption rate, animal bioassay, exposure system, finite-element method, transmission-line matrix method, computational electromagnetics, digital twin.

I. INTRODUCTION

Reverberation chambers (RCs) have been extensively employed in large-scale lifetime rodent bioassays to investigate potential dose-response relationships for a variety of cancer and non-cancer biological endpoints [1], [2], [3], [4], [5]. Studies such as those conducted by the National Toxicology Program (NTP) [6], [7] frequently require the concurrent exposure of numerous large animal cohorts at predefined target dose levels. Computational radio-frequency (RF) dosimetry plays a prominent role in study design, influencing critical choices regarding RC size, cohort spatial density, exposure levels and frequencies, as well as the interpretation of biological outcomes.

Due to the electrically-large working volumes (WVs) in rodent-loaded RCs, prior dosimetry has often relied on random plane-wave (PW) superposition techniques [8], [9] yielding idealized incident RC fields illuminating single [10], [11] or multiple numerical rodent models [12], [13], [14]. While computationally efficient, such idealized models inherently enforce artificial symmetries and neglect the physical boundary conditions (such as watering pipes, wall and

The associate editor coordinating the review of this manuscript and approving it for publication was Simone Minucci.

© 2026 The Authors. This work is licensed under a Creative Commons Attribution-NonCommercial-NoDerivatives 4.0 License.
For more information, see https://creativecommons.org/licenses/by-nc-nd/4.0/

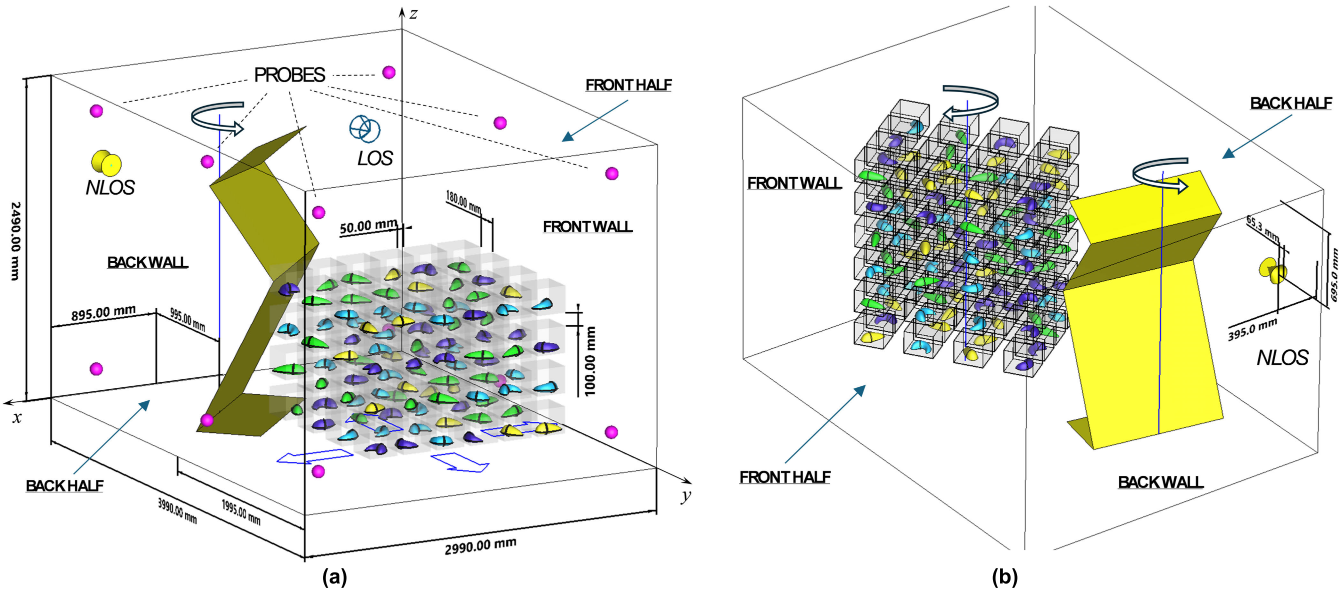

FIGURE 1. Full-wave UNIVPM-RC simulation models featuring (a) 6 × 4 × 4 static (or translational dynamic) and (b) 4 × 4 × 6 rotational dynamic cage assemblies with a discone antenna (wireframe for the LOS placement). The field probe locations are indicated by small magenta spheres in (a).

stirrer proximity) and loading effects impacting the realized field distributions in actual RCs. Consequently, only a few studies have reported full-wave characterizations of small-size [15], [16] and, more recently, large-size [17], [18] rodent-loaded RCs. This gap in the literature stems primarily from the significant computational resources required to model electrically-large cavity environments.

This study expands upon [17], [18] by incorporating RC-field sensing and intruding infrastructure within a full-wave "digital twin" methodology that simulates the complete physical geometry of a realistic facility—the Università Politecnica delle Marche (UNIVPM) RC—at 900 MHz, the exposure frequency utilized in the NTP rat bioassays. In this context, a "digital twin" is a high-fidelity numerical replica that incorporates the exact physical dimensions, structural boundaries, and realistic hardware components (e.g., stirrers, pipes) of the actual facility, distinguishing it from boundaryless PW-based models. Relying on cross-validated time-domain and frequency-domain full-wave solvers, this work addresses the "reality gap" in computational dosimetry, quantifying the statistical properties of the loaded-RC fields with the explicit inclusion of RF energy scatterers such as the RC stirrer, grounded metal pipes, and realistic antennas. Furthermore, the impact of (translational and rotational) cage-assembly dynamics aimed at improving long-term exposure uniformity across cages is evaluated, quantifying the expected mitigation of exposure imbalances.

II. MODELS AND METHODS

A. RC MODEL, EXCITATION, AND INFRASTRUCTURE

The salient characteristics of the full-wave loaded-RC model are detailed in [17] and [18], and its main aspects are summarized below. The computational domain reproduces the physical dimensions of the UNIVPM-RC, measuring approximately 3 m × 4 m × 2.5 m (x, y, z axes). The RC walls, floor, ceiling, and mode-stirrer were modeled as annealed copper ($\sigma = 5.8 \times 10^7$ S/m), modeling the internal air as a vacuum. Among practical conductors, annealed copper yields the lowest losses, thereby mitigating any confounding effects that wall losses might otherwise impose on the RC loading analysis. The loaded RC features a split-volume configuration, as illustrated in Fig. 1(a), with the antenna and rotating stirrer hosted in the back-half, while the cage assembly fits within the RC-WV in the front-half. The conformity of the UNIVPM-RC to the applicable performance standards was documented in [19].

Two cage-assembly arrangements are depicted in Fig. 1. Static and translational dynamics simulations utilized the one in Fig. 1(a), with $N = 96$ cages arranged in a regular 6 × 4 × 4 lattice (in x, y, z). By contrast, rotational dynamics simulations featured the smaller-footprint 4 × 4 × 6 lattice in Fig. 1(b). This approach maintained a steady RC loading regardless of the applied dynamics, yielding meaningful intercomparisons. The meandering watering system was simulated exclusively in the static case, approximating the NTP bioassay setups.

Overall, three antennas featuring different gains, patterns, return losses, and bandwidths were compared [18]:

- the discone antenna in Fig. 1, orthogonal to the back wall, both in a non-line-of-sight (NLOS) location relative to the cage assemblies (the stirrer limiting direct illumination), as well as in a mirrored line-of-sight (LOS) location;
- a U-shaped half-wave dipole, with its arms parallel to the RC back wall, at the same LOS and NLOS locations; and
- a large high-gain pyramidal horn squinted up and away from the cage assembly but necessarily in LOS as it could not fit in the corner behind the stirrer.

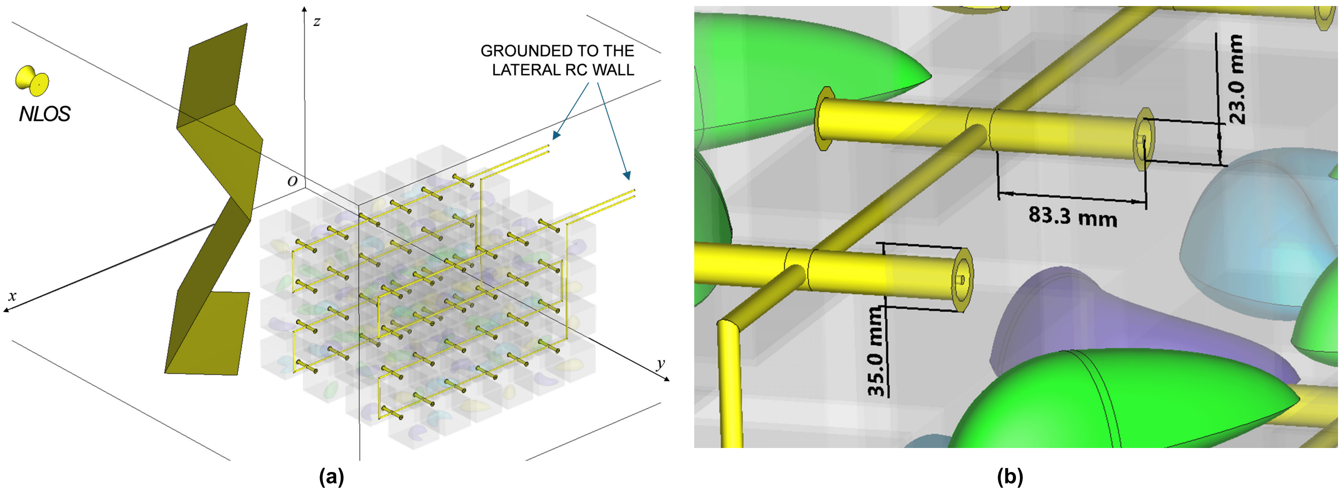

FIGURE 2. **Numerical model of the water supply infrastructure. A pair of copper serpentines provides drinking water to 48 (semi-transparent) cages each in the static assembly arrangement (6 × 4 × 4) via back-to-back quarter-wave RF-chocked sippers realized with flanged coaxial sleeves. (a) Panoramic view, illustrating the serpentines grounded to the RC lateral wall. (b) Close-up view featuring the RF-choked sipper dimensions.**

As done in [14], [17], and [18], 3 mm thick cuboidal lossless polycarbonate cages ($\varepsilon_r = 2.9$), having external dimensions 23.5 cm × 26 cm × 21 cm (in *x, y, z*) were arranged in a regular lattice with 5 cm (*x*), 18 cm (*y*), and 10 cm (*z*) inter-cage gaps. The ensuing cage assembly was positioned 30 cm above the floor and centered on the RC front-half footprint.

Translational dynamics were applied to the 6 × 4 × 4 cage assembly upon independent, uniformly random shifts along *x* and *y* axes at each next stirrer angle. Translations were bound to half-wavelength ($\lambda_0/2$) at 900 MHz in each direction along *x*, but only half such range along *y* to keep a minimum distance from the nearest wall and avoid bringing cages near the stirrer.

Rotational dynamics were applied to the 4 × 4 × 6 cage assembly through uniformly random spins about its vertical centerline, up to a full revolution, at each next stirrer angle.

Both dynamics were intentionally uncorrelated with the stepped stirrer rotation, across realizations, to preempt the onset of coherent behaviors. The uniform randomness of the realized dynamics was verified from simulation records.

1) CHOKED WATER PIPING MODELING

A critical requirement for lifetime bioassays is the continuous provision of clean drinking water. To prevent RF energy absorption by the water from degrading the RC exposure efficiency, the water is delivered through metal pipes, which can be RF-grounded to the RC walls. Consistent with the adoption of the NTP bioassay cage dimensions and assembly, the water delivery system was modeled after the meandering NTP design [6], [7]. As illustrated in the panoramic view in Fig. 2(a), the simulated infrastructure consisted of annealed copper piping grounded to the RC lateral wall. This system features two serpentines, each equipped with 24 back-to-back flanged quarter-wave RF chokes, delivering water to all 96 rodents. As detailed in Fig. 2(b), these chokes surround back-to-back sipper valves serving opposite cages, to limit the RF contact currents during water intake. Because the present simulations did not feature rodent models in a drinking posture (i.e., touching the metal sippers), the ceramic grommets used in the physical NTP setup to provide spacing from the flanges were omitted without impacting the wbSAR results. This intruding watering system was implemented exclusively in the static cage assembly (6 × 4 × 4) to reflect the static NTP setups.

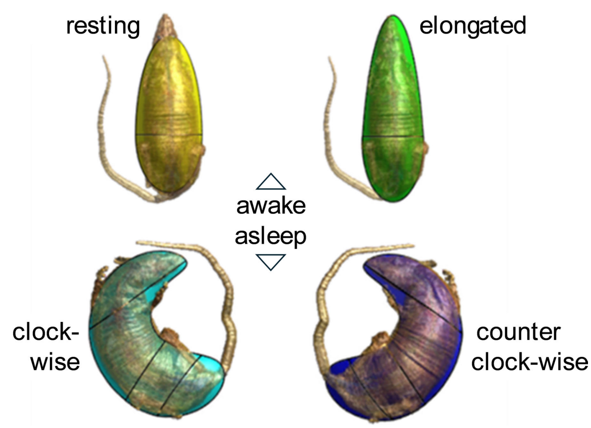

FIGURE 3. **The four homogeneous phantom postures employed in the simulation: resting, elongated, asleep (clockwise or counter-clockwise), compared against the respective anatomically-correct rat models used to validate them. Figure adapted from [14].**

B. RODENT MODELS AND COHORT GENERATION

The UNIVPM-RC "digital twin" was loaded with 96 homogeneous, randomly postured tail-less rat phantoms ($\rho = 1000$ kg/m^3; $\sigma = 0.95$ S/m, $\varepsilon_r = 40$ at 900 MHz), previously validated against anatomically-correct models [14]. Figure 3 illustrates the four postured models utilized in the simulations (resting, elongated, clockwise, or counter-clockwise asleep).

For a given cohort mean weight between 450 g and 750 g, an equiprobable random posture is assigned to each phantom, which is then scaled to a random weight drawn from a raised-cosine distribution with a 12% relative standard deviation (R-SD) derived from published NTP datasets for adult male rats. The 450 g - 750 g simulated range was chosen to be symmetric relative to the expected (550 g) and observed ($\sim$ 650 g) ranges during the second year of the NTP male rat bioassays [6].

Similar to the "day-long" exposure scenario in [14], at each consecutive stirrer angle, the rat phantoms were placed on their respective cage floors with a uniformly random rotation in $[0,2\pi)$ about a vertical abdominal axis, and subjected to uniformly random translations along x and y within the cage boundaries. However, a critical methodological distinction from [14], however, lies in the mass assignment. In [14], the phantom mass was kept fixed in each cage across all stirrer angles (yielding cage-wise time-averaged wbSARs), whereas in this study, the mass was randomly reassigned at each successive stirrer angle to generate cage-wise ensemble wbSAR statistics. This choice allows to disentangle the cage location effects from phantom mass effects, while reflecting typical animal rotation practices (e.g., the twice-weekly cage rotations employed in the NTP rodent bioassays [6]).

C. FIELD MONITORING PROBES

In large-scale bioassays, RF dosimetry is essential to establish the relationships between external exposure metrics (e.g., incident RF power density) and internal dosimetric quantities (e.g., whole-body average SAR). For instance, the NTP rodent setups featured two diode-detector field probes per RC to control the mean cohort wbSAR via feedback readings to the RF power generating system every 20 s [6].

To emulate this field sampling within the loaded-RC "digital twin", a network of $N_P = 12$ isotropic point field probes was implemented to record both electric and magnetic field waveforms. As depicted in Fig. 1(a), these probes were positioned $\frac{3}{4}\lambda_0$ (at 900 MHz) away from the nearest RC walls, at the eight RC corners and the four corners of the midplane between the RC halves. These probe locations are identified using a three-part positional convention based on: longitudinal placement ("ant" for the back-wall corners by the antennas, "mid" for the midplane, "far" for the front-wall corners), height ("Top" for ceiling, "Btm" for floor), and lateral x-coordinate ("Xm" for the lower and "Xp" for the higher coordinate). Notably, none of these simulated probes were positioned within the cage assembly itself, as such placement would be operationally impractical given the daily movement of cages and the animal handling required in a physical facility. Ultimately, sampling both fields at multiple distributed locations helps in assessing the likelihood of local biases (e.g., artificially elevated readings) due to antenna type and (N)LOS placement, guiding the optimal selection of the physical probe locations and associated field types.

D. NUMERICAL METHODS AND SOLVER SELECTION

The loaded-RC simulation models were implemented in Dassault Systèmes SIMULIA CST Studio Suite 2025, using embedded Visual Basic scripting to effect the aforementioned randomizations. CST Studio Suite allows for the execution of the same "digital twin" model using both time- and frequency-domain solvers; the Transmission Line Matrix (TLM) method was employed for the former and the Finite Element Method (FEM) for the latter. In both cases, the RF excitation was modeled as a lumped linear 50 Ω source.

Most simulations utilized wideband TLM setups featuring a filtered, DC-free excitation waveform over the 0-1.2 GHz range. Conversely, single-frequency FEM simulations at 900 MHz, featuring mesh adaptation driven by the convergence of wbSARs in each phantom [17], were employed to cross-validate select TLM results. This is an essential step, as no experimental validation was planned. Because the FEM simulation parameters and the FEM-TLM cross-validation have been detailed in [17] and [18], respectively, only the TLM simulation results at 900 MHz are discussed herein. Exhaustive solver configurations and validation parameters mirror those detailed in prior work [17], [18].

TABLE 1. GPU-equipped servers employed for all TLM simulations (Motorola Solutions, Fort Lauderdale, USA).

ID	OS	CPU	RAM	GPU
Twain	Red Hat Enterprise Linux 9.2	2x96 cores @ 3.20GHz	2 TB	1x H100 NVL
Kafka			256 GB	4x P100-PCIE-16GB
Plato-α	Windows Server 2016	1x16 cores @ 2.60GHz	512 GB	2x A100-PCIE-40GB
Plato-β				
Hugo	Windows 11 Pro 24H2	1x14 cores @ 2.60GHz	256 GB	4x P100-PCIE-16GB
Dante		2x10 cores @ 2.20GHz	96 GB	1x V100-FHHL-16GB

All servers engaged in the TLM simulations, detailed in Table 1, featured at least one NVIDIA Graphics Processing Unit (GPU). Typical runtimes ranged from 3 to 5 h per stirrer angle, requiring approximately one week on average to complete a stirrer revolution, at 10° increments.

E. TRIAL CASES

The results presented in Section III encompass 22 trial cases, listed in Table 2, categorized by physical environment, cage assembly dynamics, antenna configuration, and cohort-mean mass. For each stirrer angle, the instantaneous field readings and computed wbSAR values were initially normalized to the antenna instantaneous net input RF power. Alternative normalizations were also performed with respect to estimates, derived by averaging the squared field magnitudes across all

TABLE 2. Simulated environments, dynamics, antenna configurations, and the corresponding cohort masses available for analysis (twenty-two datasets, each encompassing 36 stirrer positions with 10° step - total 792 TLM simulations).

Water piping	Dynamics	Antenna configuration	Mean cohort weight
Yes	Static	Discone NLOS	450 g, 550 g, 650 g, 750 g
		Discone LOS Horn LOS U-dipole NLOS & LOS	650 g
No	Static	Discone NLOS	450 g, 550 g, 650 g, 750 g
		Discone LOS Horn LOS U-dipole NLOS & LOS	650 g
	Rotational	Discone NLOS & LOS Horn LOS U-dipole NLOS & LOS	
	Translational	Discone NLOS	

12 probes, of the volumetric RF energy density, and to the incident squared $\boldsymbol{E}$-field magnitude averaged across probes.

To systematically evaluate exposure imbalances, the cages were categorized using two spatial grouping schemes. The first scheme was based on the topological position within the assembly lattice: *corner* (C), *edge* (E), *face* (F), and *inner* (I) cages. The second is based on the longitudinal distance from the mode-stirrer (layers A, B, C, D), where Layer A comprises the cages closest to the stirrer (near the RC midplane) and Layer D those farthest from it (near the front wall).

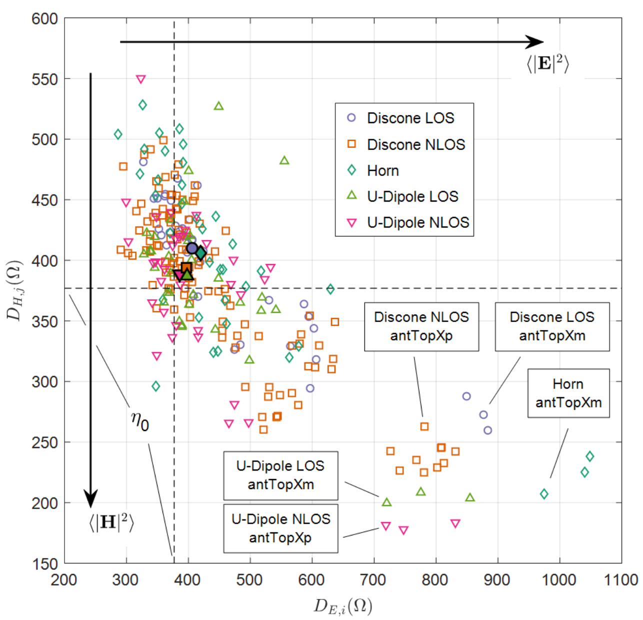

FIGURE 4. Probe dominance chart relative to the datasets in Table 2. Each mark represents a particular probe for a certain loaded-RC configuration (cage assembly dynamics; mean cohort weights;with or without water piping). Marker colors identify the corresponding antenna configurations, with filled markers representing the respective median centers. Specific labels are displayed for the most extreme outliers.

III. RESULTS

Two environmental configurations served as baselines, both featuring the static cage assembly to closely resemble the setups in [4]: one with and one without the serpentine water piping threading the cage lattice. Translational and rotational dynamics were applied exclusively to the latter case since the movements were unrestricted by the water delivery system. A quantitative evaluation of the dosimetric impact of the water-supply piping is provided in Table 5 and illustrated in Fig. 7.

To quantify the antenna type and placement effects, the Discone NLOS was set as the reference configuration and simulated across the full spectrum of cohort weights in both baseline environments. The pyramidal horn antenna was studied due to its very directive pattern, whereas the U-shaped half-wave dipole antenna was selected owing to the absence of deep radiation pattern nulls in free space. A comparative

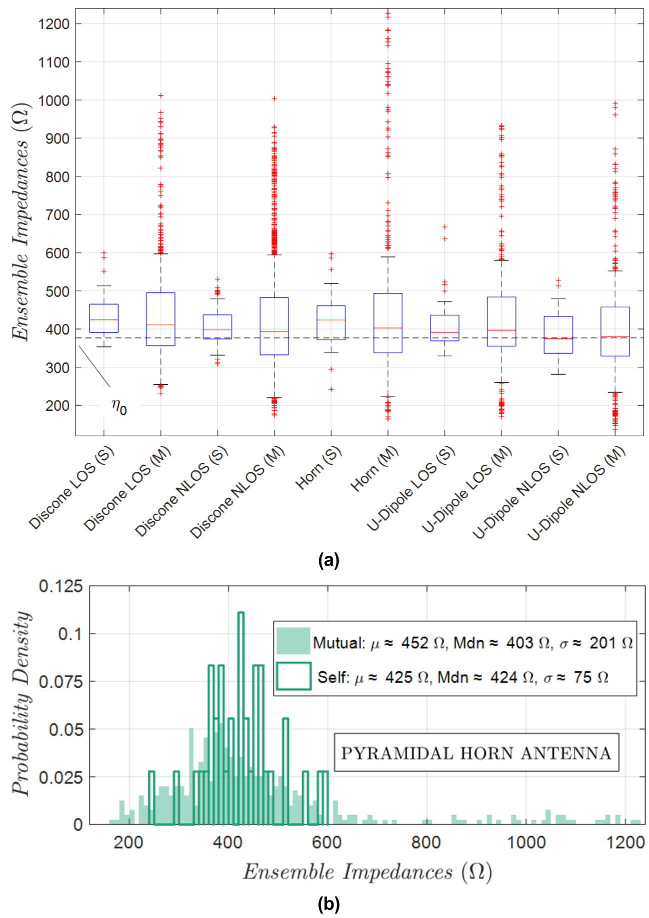

FIGURE 5. Statistical distributions of (a) loaded-RC self (S) and mutual (M) ensemble impedances. The dataset encompasses all antenna configurations, cage assembly dynamics, mean cohort weights, and infrastructure scenarios (with or without water piping). Box-and-whisker plots indicate the median, interquartile range (IQR), and tight whisker limits (0.75 × IQR), with outliers plotted individually. (b) Histograms illustrating the broadest mutual impedance spread observed (horn).

analysis of all five antenna configurations in Table 2 was conducted using the 650 g benchmark mean-cohort weight.

A. RC FIELD IMPEDANCE STATISTICS

While standard calibration protocols (IEC 61000-4-21) requires eight probes to check the field uniformity inside the chamber [20], in the present case 12 probes were considered to study the presence of a large biological load, that inevitably degrades its modal structure. To examine this deviation, the loaded-RC simulated field properties were benchmarked against the theoretical framework for well-stirred fields [21].

In ideal Rayleigh fields, the ratio between the ensemble average of the squared electric field magnitude at an arbitrary point in space and the ensemble average of the squared magnetic field magnitude, at the same, or at any other point, results in the free-space impedance ($\eta_0 \approx 377\ \Omega$) squared. The 12 simulated probe waveforms yield the field magnitudes at each probe location, across stirrer angles, at $f_0 = 900\ MHz$, further yielding the *ensemble impedance matrix*

$$\eta_{i,j} = \sqrt{\frac{\langle |\boldsymbol{E}(f_0)|_i^2 \rangle}{\langle |\boldsymbol{H}(f_0)|_j^2 \rangle}},\ i,j = 1,2,\cdots,12, \qquad (1)$$

where $\eta_{i,j}$ denotes the impedance terms, and $\langle\cdot\rangle$ stands for the ensemble average across stirrer angles. The matrix main diagonal encompasses the ensemble self-impedances, while off-diagonal elements represent ensemble mutual-impedances. Self-impedances depend on the local field structure at each probe location [22], which is influenced by the immediate surroundings, so anomalies usually point to local issues (e.g., a standing-wave peak). In contrast, mutual impedances describe how the $\boldsymbol{E}$-field readings at one location relate to the $\boldsymbol{H}$-field elsewhere, pointing to a global behavior.

To isolate probe-location anomalies, the global impact on the mutual impedances was quantified using the row medians for the $\boldsymbol{E}$-field and the column medians for the $\boldsymbol{H}$-field, excluding self-impedances. For example, a large median value in the jth column would indicate unusually low $\boldsymbol{H}$-field readings at the jth probe, affecting all the mutual impedances in which the remaining probes provide the $\boldsymbol{E}$-field readings. This metric, which effectively filters out local electromagnetic energy variations, highlighting probes with systematic bias, can be formalized by introducing the following $\boldsymbol{E}$*-dominance* and $\boldsymbol{H}$*-dominance* scores:

$$D_{E,i} = \text{median}_{i\neq j}\left(\eta_{i,j}\right),\ D_{H,j} = \text{median}_{i\neq j}\left(\eta_{i,j}\right),\quad i,j = 1,2,\cdots,12. \qquad (2)$$

For a given RC configuration, a dominant $\boldsymbol{E}$-field probe would be reading consistently higher, whereas a dominant $\boldsymbol{H}$-field probe would read lower, than the collective median. Therefore, a *probe dominance chart* may be defined wherein each probe is located by the coordinates given by its own $\boldsymbol{E}$-dominance and $\boldsymbol{H}$-dominance scores. Since the ensemble mutual impedances do not depend on the net input RF power, plotting these dominance scores, as shown in Fig. 4 for all the trial cases in Table 2, allows the visual identification of probes characterized by anomalous readings. For each antenna configuration ensemble-impedance matrix, the filled markers correspond to the median mutual impedance, all being quite close to the ideal value η_0 (dashed lines). Dominance scores farther away from the respective medians indicate probes featuring unusually large or small readings, depending on the quadrant in which they fall.

Notable outliers occur at high field values for both $\boldsymbol{E}$- and $\boldsymbol{H}$-readings near the antennas, as shown by the probe/antenna labels in quadrant IV, suggesting strong localized RF energy density. Most dominance scores tend to scatter over quadrants II and IV, indicating concurrently lower or higher field value readings for both $\boldsymbol{E}$- and $\boldsymbol{H}$, while significantly fewer exhibit moderate imbalances between the fields (quadrants I and III).

Table 3 reports the statistical parameters (mean μ, median Mdn, and standard deviation σ) of the ensemble impedance distributions across antenna configurations. Both metrics appear generally proximate to η_0, confirming the statistical uniformity of the loaded RC, with the mutual impedances (ratios of uncorrelated $\boldsymbol{E}$- and $\boldsymbol{H}$-fields) featuring greater variability than self-interactions (local fields). Indeed, in the box-and-whisker plots in Fig. 5(a) the self-impedances remain tightly clustered, whereas the mutual impedances clearly feature heavier tails with numerous outliers. To apply a strict self-impedance goodness criterion, tighter whisker limits (0.75 × IQR, inter-quartile range) than in conventional Tukey box plots (1.5 × IQR) were enforced.

TABLE 3. Statistical comparison of self and mutual ensemble impedances across the antenna configurations listed in Table 2.

Antenna configuration	Type	μ (Ω)	Mdn (Ω)	$\sigma_{self\,/\,mutual}$ (Ω)	$\frac{\sigma_{mutual}}{\sigma_{self}}$
Discone LOS	Self	434.1	424.6	60.9	2.50
	Mutual	451.3	411.2	152.2	
Discone NLOS	Self	406.6	397.6	47.6	3.03
	Mutual	425.3	392.8	144.3	
Horn	Self	425.0	423.9	74.8	2.69
	Mutual	451.7	403.2	200.8	
U-dipole LOS	Self	415.3	391.7	76.4	1.85
	Mutual	430.0	397.0	141.4	
U-dipole NLOS	Self	386.4	374.7	62.8	2.29
	Mutual	405.1	380.5	144.0	

TABLE 4. Probe locations with at least one ensemble self-impedance outlier across the antenna configurations listed in Table 2.

Probe label	Discone		Horn	U-dipole	
	LOS	NLOS		LOS	NLOS
antBtmXm	—	—	1	1	—
antTopXm	3	6	2	—	—
antTopXp	—	3	—	—	—
farBtmXm	—	2	2	3	—
farBtmXp	—	1	—	—	—
farTopXm	—	—	—	1	—
farTopXp	—	—	—	—	2

As detailed in Table 3 and visually captured by the histogram in Fig. 5(b), the most directive antenna (horn) shows the largest mutual impedance spread with $\sigma_{mutual}/\mu_{mutual} \approx$

0.44, while all others are around 0.33. Hence, the horn antenna directionality likely induces sharper standing wave patterns (stronger "hot spots" and deeper "nulls") compared to omnidirectional antennas, especially if the RC is far from perfectly stirred. This increased spatial variance naturally manifests as a wider mutual impedance spread.

Furthermore, the granularity afforded by the loaded-RC simulation allows spotting probe locations prone to self-impedance outliers, relative to the whole ranges associated with the respective antenna configurations. Figure 6 illustrates two instances where specific probe locations feature multiple outliers. Finally, Table 4 details all probe locations where at least one outlier was detected across antenna configurations, directly correlating with the outliers observed in the self-impedance box plots in Fig. 5(a). Ultimately, a wider impedance spread indicates the presence of highly localized RF energy peaks and valleys that could severely compromise the required dose uniformity across the bioassay cohort.

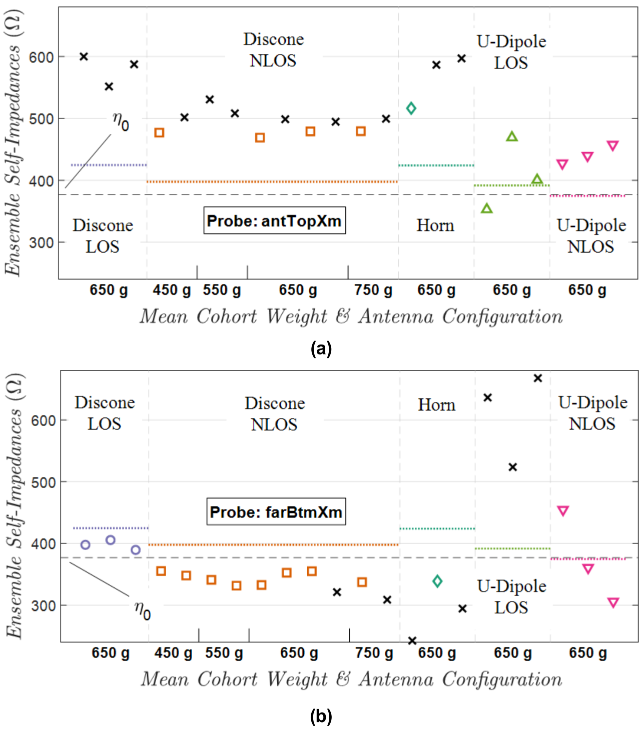

FIGURE 6. Ensemble self-impedances at two exemplary probe locations, across all the RC configurations in Table 2. Outliers ("X") are derived from each antenna configuration self-impedance distribution. While in (a) the "antTopXm" location presents large outliers except for the U-dipole, in (b) the "farBtmXm" location features either small or large outliers for all antenna types. Dotted lines represent the median values, across all probes, for each antenna configuration.

B. DOSIMETRIC FACTOR

To accurately control the RF exposure levels in a large-scale bioassay, a reliable transfer function between the external electromagnetic environment and the actual power absorbed by the biological models is typically quantified as

$$\mathrm{DF} \overset{\mathrm{def}}{=} \frac{\frac{1}{N}\sum_{h=1}^{N}\langle \mathrm{wbSAR}_h\rangle}{\left\langle \frac{1}{N_P}\sum_{j=1}^{N_P}\left|\mathbf{E}_j\right|^2/2\right\rangle}, \tag{3}$$

where DF is a *dosimetric factor* linking ensemble-averaged, cohort-mean wbSAR across all N cages to ensemble-averaged squared *rms* $\boldsymbol{E}$-field magnitudes from all N_P probes. Note that cage-wise wbSAR ensemble averaging, related to longer time scales and therefore the expected thermal load, is carried out first, yielding the $\{\langle \mathrm{wbSAR}_h\rangle\}$ set; the cohort-wide averaging over the N cages (or, alternatively, the median) follows.

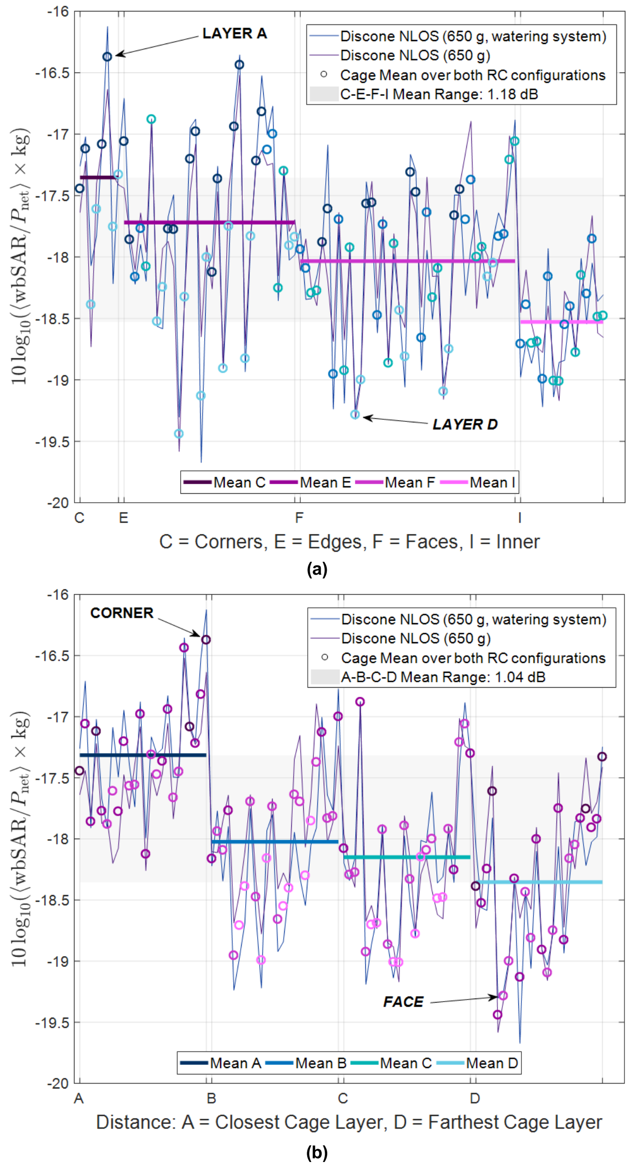

FIGURE 7. Ensemble-averaged wbSAR per cage (discone NLOS, 650 g), normalized to net input RF power, compared with and without water piping. Data ordered by (a) topological cage lattice category (C-E-F-I) and (b) cage layer distance from the RC stirrer (A, B, C, D). Horizontal segments indicate categorical means across locations and distances, with corresponding dB-ranges listed in the legends. Scatter plots show cage-wise means across both cases, with marker and segment colors cross-referencing topological and spatial layers (the labeled examples refer to a corner cage on Layer A and a face cage on Layer D).

The baseline RC configuration without water piping or dynamics (650 g mean weight), which is most similar to those studied using PW superposition, features

DF $\approx 32.6\ (\mu W/kg)\ /\ (V/m)^2$, versus $45.2\ (\mu W/kg)\ /\ (V/m)^2$ (mean cohort wbSAR $\approx$ 0.2261 W/kg with 5000 V^2/m^2 time-averaged incident $\boldsymbol{E}$-field squared *rms* magnitude) for the "day-long" exposure scenario in [14]. This moderate gap can be attributed to inherent PW-model approximations, such as the inability to account for realistic RC loading effects, as well as its unavoidable reliance on load-less "empty-chamber" incident fields for DF estimations.

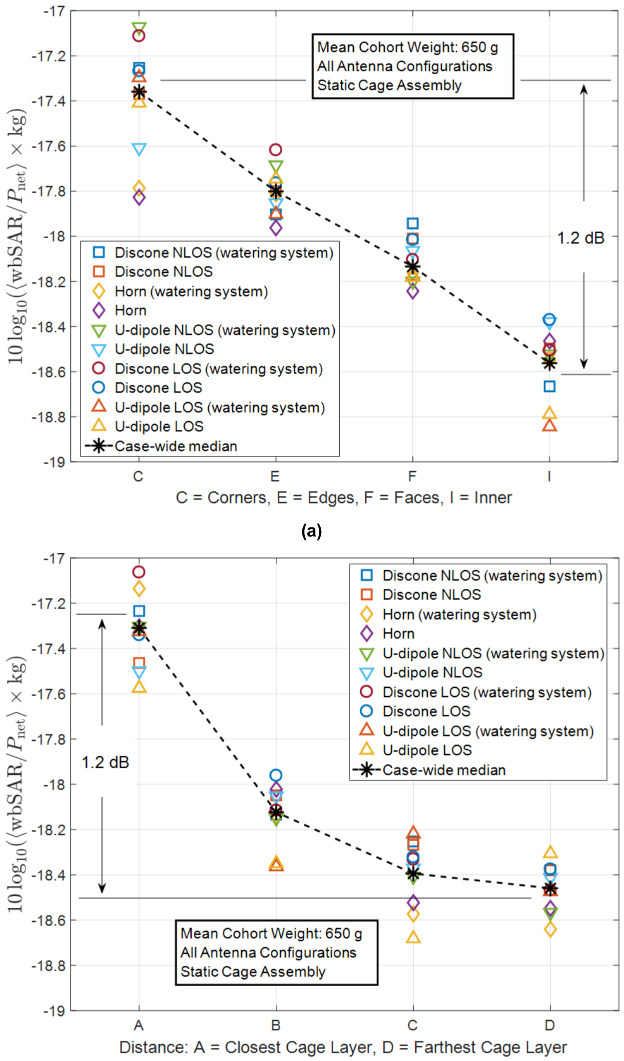

FIGURE 8. **Medians of the cage-wise, ensemble-averaged wbSAR for the 650 g cohort (normalized to net input RF power, across all antenna configurations). Data ordered by (a) topological cage lattice category (C-E-F-I), and (b) cage layer distance from the RC stirrer (A-B-C-D). Scatter-dash lines connecting case-wide medians show the categorical trends.**

C. CAGE-WISE WHOLE-BODY SAR IMBALANCES

The PW-superposition model presented in [14], featuring the 6 × 4 × 4 baseline cage assembly with a 650 g mean cohort weight, did not reveal significant imbalances ($\approx$ 5% in terms of time-averaged wbSAR for the "day-long" exposure scenario) among the C-E-F-I cages. Rayleigh incident fields synthesized through PW superposition feature inherent symmetries, while the cage assembly is symmetric about its mid-planes, thus limiting the degrees of freedom in terms of exposure asymmetries compared to a realistic RC model (even more so when considering intruding scatterers like the RF-choked watering infrastructure). A cage-wise asymmetry characterization is therefore warranted.

TABLE 5. **Maximum cage-wise imbalance, in terms of ensemble-averaged whole-body SAR, for the static RC configurations with the discone (NLOS) antenna configuration.**

Water Piping	Cohort mean weight			
	450 g	550 g	650 g	750 g
Yes	2.87 dB	3.46 dB	3.55 dB	3.80 dB
No	3.18 dB	2.83 dB	3.06 dB	3.33 dB
dB-difference	-0.31 dB	+0.63 dB	+0.49 dB	+0.47 dB

Because the baseline RC configuration is the most suitable for comparison with the PW-superposition results from [14], it was characterized both with and without the metal piping. This cage-wise exposure asymmetry characterization was expanded to include all cohort mean weight cases (listed in Table 2) and is reported in Table 5 in terms of dB-differences between maximum and minimum ensemble-averaged wbSARs across cages. These results show larger exposure asymmetries ($\approx$ 3dB) compared to the PW-based results ($\approx$ 1.7dB, from Fig. 12 in [14]). Furthermore, the presence of the metal piping increased this asymmetry by approximately 0.5 dB, except for the lowest weight group, where the effect is reversed, yet small, indicating lower interaction with the RF-choked sippers for smaller rodents (non-drinking postures).

Figure 7 reports the corresponding cage-wise ensemble-averaged wbSARs, normalized to the net input RF power. In contrast to PW-superposition incident fields (see Table 4 in [14], "day-long" scenario), the loaded-RC results in Fig. 7(a) reveal an $\approx$ 1.2dB wbSAR average spread between corner (C) and inner (I) cages, with edge (E) and face (F) cages falling in between. The results in Fig. 7(b) quantify the impact of the cage distance from the stirrer, showing $\approx$ 1dB decrease, on average, between those closest (A) and farthest (D) cages. The inherent symmetries imposed by PW-synthesized Rayleigh fields in [14] could not unveil such imbalances.

The color-coding of the scatter circles cross-references the spatial distance layers in Fig. 7(b) with the topological categories in Fig. 7(a), and vice versa. This representation provides visual hints of how cage location and distance from the stirrer compound create the large cage-wise imbalances documented in Table 5. It also helps explain the mentioned gap ($\approx$ 1.7 dB compared to $\approx$ 3 dB spread) between PW-based and loaded-RC simulated wbSAR ranges.

The baseline configuration trends observed in Fig. 7 are confirmed across all antennas, both with and without watering system, as shown by the medians of the ensemble-averaged, cage-wise wbSARs for the C-E-F-I and A-B-C-D cage groups in Fig. 8. Here, the cohort-wise medians are

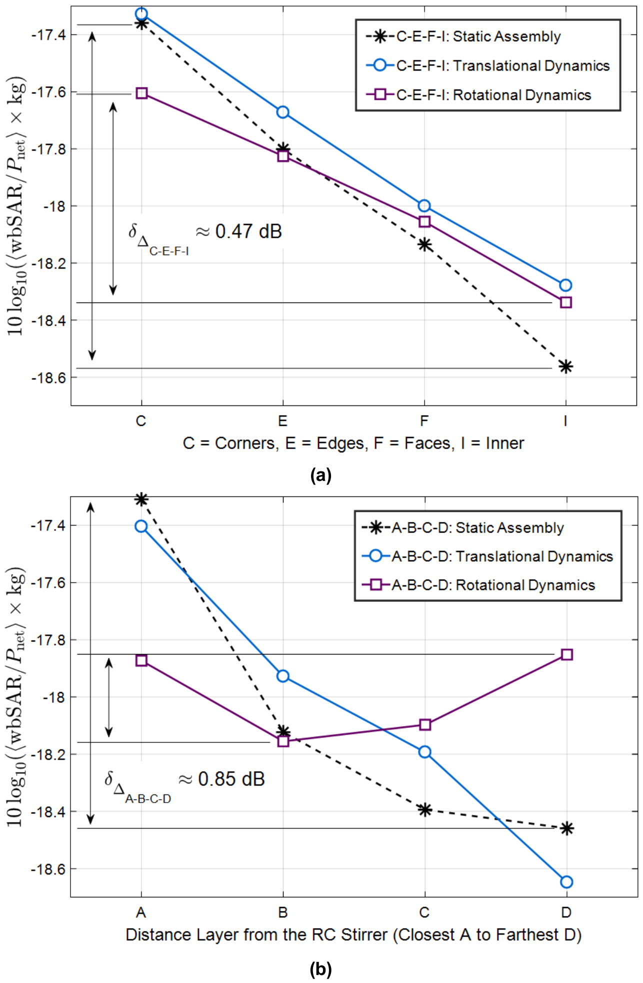

FIGURE 9. **Exposure imbalance mitigation for (a) cage location category and (b) distance layer via translational and rotational cage assembly dynamics (antenna configurations with 650 g mean cohort weight). Data points are cage-group medians of the respective ensemble-averaged wbSAR normalized to the antenna net input RF power. The dB figures in each plot represent (a) category-wise and (b) distance-wise imbalance improvements between static and rotational dynamics, respectively.**

the appropriate statistical descriptors, even though the cage-wise, ensemble-averaged wbSARs remain the biophysically relevant metric acting as a suitable proxy for thermal load. As shown in Fig. 8, all configuration-specific medians accumulate along similar trends with respect to the cage topological locations (Fig. 8a) and distances (Fig. 8b). The respective interpolated trends (scatter-dashed lines) clearly illustrate the dominant influence of these categories on the resulting thermal load imbalances.

1) EXPOSURE IMBALANCE MITIGATION VIA CAGE DYNAMICS

Translational and rotational cage assembly dynamics were applied to mitigate the wbSAR imbalances observed in the aforementioned baseline cases. Figure 9 reports the median ensemble-averaged wbSAR values across the C-E-F-I and A-B-C-D categories. Scatter-dashed plots denote all the static configurations presented in Fig. 8 (10 cases across all antenna configurations, see Table 2), while square and round scatter-marks indicate rotational (5 cases) and translational (a single trial case) dynamics, respectively. Whereas translational dynamics proved ineffective at addressing the exposure imbalances (hence the single trial), applying rotational dynamics yielded measurable improvements over both cage group categories. In particular, an ≈ 0.47 dB improvement was observed across topological cage locations, as shown in Fig. 9(a), alongside an ≈ 0.85 dB improvement across the distance layers, as seen in Fig. 9(b). The combined effect produced around 1 dB overall improvement.

As shown in Table 6, expanding the rotational dynamics analysis of the baseline RC model (650 g, no watering system) to encompass every antenna configuration resulted in exposure imbalance reductions in the $0.88 - 2.45$ dB range.

TABLE 6. **Maximum cage-wise ensemble-averaged wbSAR imbalance for static and rotational dynamics across antenna configurations (650 g mean cohort weight, without watering system).**

Cage Assembly Dynamics	Antenna configuration				
	Discone		Horn	U-Dipole	
	LOS	NLOS		LOS	NLOS
Static	3.03 dB	3.06 dB	4.56 dB	3.97 dB	2.48 dB
Rotational	1.53 dB	1.94 dB	2.11 dB	3.06 dB	1.6 dB
dB-difference	1.50 dB	1.12 dB	2.45 dB	0.91 dB	0.88 dB

2) IMPACT OF wbSAR NORMALIZATION ON THE THERMAL LOAD

Full-wave loaded-RC modeling allows the investigation of how different SAR normalization metrics impact the expected variance of actual exposures. In particular, the effect on the ensemble-average wbSAR, which impacts the thermal load imposed on the rodents, may be physiologically relevant.

Because the reactive RF energy distribution in the chamber and the RF losses in the rodents vary with the stirrer angle, the relationships between sparsely probed energy quantities and the net RF input power at the antenna feed, as well as the RF loss in the animals and any other RC fixture, are not invariant.

In the context of monitoring exposures in real time, the impact of normalizing the instantaneous wbSARs with respect to the instantaneous net input RF power, total RF energy density, or squared electric field should be addressed. In Table 7, such an impact was quantified in terms of the relative standard deviations of instantaneous and ensemble-averaged cage-wise wbSARs, for the static cage assembly and across dynamics (discone NLOS, no water piping, 650 g). As shown, applying rotational dynamics significantly improves the ensemble-averaged wbSAR spread across cages, reducing the R-SD to $\approx 10\%$ regardless of the chosen normalization metric. The larger variance observed for the case of energy-normalized instantaneous wbSAR, compared to net power normalization, can likely be attributed to the higher variability of the RC energy density estimate (and even more so for the squared $\boldsymbol{E}$-field) derived from sparse 12-probe field sampling. Evidently, the net input RF

TABLE 7. Effects of cage assembly dynamics on the instantaneous and ensemble-averaged wbSAR relative standard deviation for all considered normalizations (discone NLOS, no water piping, 650 g mean cohort weight with 12% raised-cosine distribution R-SD).

Cage Assembly		R-SD of the wbSAR normed relative to					
		Net RF input power at feed-point		RF energy density (12-probe avg.)		Squared ***E***-field (12-probe avg.)	
Dynamics	Layout	Instantaneous	Ensemble Avg.	Instantaneous	Ensemble Avg.	Instantaneous	Ensemble Avg.
Static	6 × 4 × 4	40.4%	14.6%	44.3%	14.8%	47.1%	15.0%
Translational		40.2%	14.1%	45.3%	14.5%	49.6%	14.5%
Rotational	4 × 4 × 6	39.8%	10.1%	42.9%	10.0%	46.4%	10.1%

power serves as a more stable proxy for the mean-cohort wbSAR than sparsely sampled energy quantities, particularly since the RF losses in the RC model used in this study occur almost entirely within the rats.

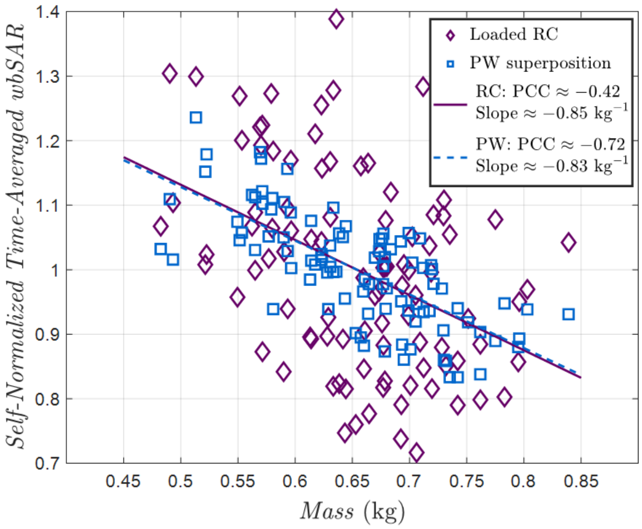

FIGURE 10. Mass-dependent wbSAR variability comparing idealized and realistic dosimetry models (650 g cohort, 6 × 4 × 4 static assembly, discone NLOS, no watering pipes). PW-based time-averaged wbSARs [14] are overlaid on loaded-RC results ("day-long" scenario, constant mass in each cage), with respective datasets normalized to their cohort-wide means. Despite overlapping trendlines, the loaded-RC model yields significantly weaker mass-dose interdependency (PCC ≈ −0.42) than the PW-based prediction (PCC ≈ −0.72).

D. MASS-WBSAR SENSITIVITY AND CORRELATION

Using the Pearson correlation coefficient (PCC), PW-based modeling reported a strong negative mass-dose correlation (PCC ≈ -0.72) for the time-averaged wbSAR [14, Fig. 13]. In contrast, the baseline loaded-RC simulations (discone NLOS, static arrangement, no watering system, 5° stirrer steps, 650 g) revealed significantly weaker correlation when replicating the "day-long" exposure scenario (constant mass per cage) [14].

Figure 10 compares the PW-based results [14] (2500 field realizations) against the loaded-RC (72 realizations); while the trendlines overlap, the loaded-RC exhibits markedly higher variance (PCC ≈ -0.42). To isolate this mass-dose effect from probe sampling spread (Table 7), the loaded-RC wbSARs were normalized to net input RF power before normalizing each dataset to its cohort-wide mean. The loaded-RC results were insensitive to the number of realizations (stirrer angle step), yielding PCC ≈ -0.44 with 10° increments.

While Fig. 10 reflects constant cage-wise masses for direct comparison with [14], the proposed methodology randomizes mass assignments per stirrer realization, thereby introducing a statistical challenge: the ensemble-averaged randomized mass converges toward the cohort mean (650 g), rendering mass-wbSAR correlation mathematically degenerate in the limit.

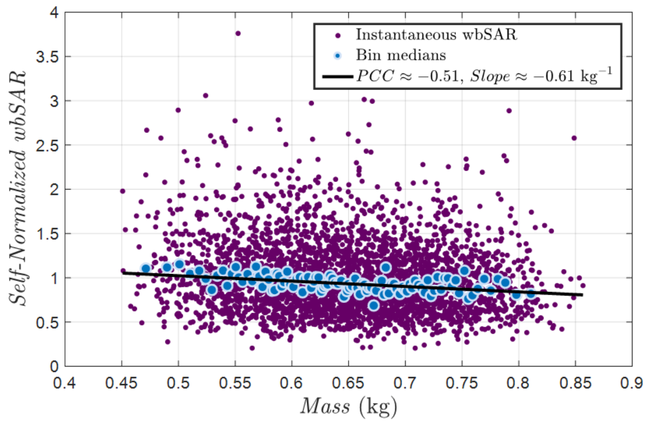

FIGURE 11. Equal-frequency binning regression for the baseline loaded-RC (discone NLOS, 650 g). Raw instantaneous wbSARs (purple dots) are filtered into bin medians (blue circles) to mitigate lognormal outliers. A linear fit applied exclusively to these medians captures the central mass-dose correlation. Fit parameters are listed in the legend.

Conversely, applying least-squares linear regression directly to instantaneous wbSAR data introduces artifacts. Unaveraged wbSARs are lognormally distributed [4], [5], which artificially pulls the regression trendline upward and distorts the mass-dose relationship. To resolve this, an equal-frequency binning method was implemented. Raw instantaneous (mass, wbSAR) pairs were sorted by mass and partitioned into 100 equal-sized bins to ensure consistent statistical power. Computing the median wbSAR within each bin inherently filters out lognormal outliers, allowing a linear regression of these medians to reliably capture the central tendency reliably. Figure 11 demonstrates this binning approach for the baseline loaded-RC configuration with fully randomized mass assignments. Regression exclusively on the bin medians yields a normalized slope of -0.608 kg^{-1} (PCC ≈ -0.51), corroborating the constant-mass findings in Fig. 10.

IV. DISCUSSION

This study advances computational dosimetry for large-scale rodent bioassays by employing a full-wave "digital twin" of a loaded RC. Until the last decade, the computational burden of simulating electrically large, heavily loaded cavities made such full-wave modeling largely impractical. For the most part, prior dosimetry necessarily relied on idealized PW-superposition methods. The transition to detailed realistic simulations reveals exposure nuances previously obscured by the inherent symmetries of those foundational PW models.

A primary outcome of this work is the quantification of the "reality gap" in the assessment of the RF exposure uniformity. While comparable PW-based studies [14] estimated cage-wise wbSAR imbalances around 1.7 dB, loaded-RC simulations accounting for physical boundaries and energy damping reveal imbalances exceeding 3 dB. The inclusion of metallic water piping was found to further exacerbate these imbalances by about 0.5 dB, especially for larger rodents (even absent a "drinking posture"). Reliable modeling this sort of intrusive infrastructure allows anticipating exposure imbalances before physical construction, giving a chance to devise mitigations.

A significantly weaker correlation than predicted by PW-superposition was observed between the ensemble-averaged wbSAR and rodent mass within a specific weight group. In a realistic RC environment, stochastic field variations at specific cage locations overwhelm the mass-dependent absorption effect. Consequently, a heavier rat does not necessarily receive a lower dose than a lighter one; dose is primarily dictated by cage location. The biophysical implication is that larger rodents placed in high-exposure cages may experience higher thermal core temperatures than previously understood due to their greater volume-to-surface ratio. Such a potential thermal load confounder remains unmitigated by higher mass.

The results documented unintuitive effects of antenna type and position on exposure imbalances and probed RC field readings, suggesting that full-wave loaded-RC simulations may provide room for optimization at the design stage.

To mitigate spatial imbalances, rotational cage dynamics proved highly robust, reducing maximum imbalances from over 3 dB to ~1.5–2.1 dB. Integrating a continuous watering system into a rotational setup may be practically achievable, for instance, by routing supply lines along the rotation axis.

Finally, relying strictly on net-input RF power for wbSAR normalization was shown to be reliable, at least if extraneous RF losses are negligible. Because this is rarely true in lifetime bioassays due to daily fluid loss and food presence, reliable dosimetry requires linking external field energy metrics to SAR metrics. However, utilizing a sparse subset of monitoring probes was shown to be vulnerable to significant estimation uncertainties. These aspects of normalization and optimal probe selection will be addressed in a separate publication.

V. CONCLUSION

This work establishes a comprehensive full-wave numerical dosimetry framework for large-scale rodent bioassays. By rigorously modeling the antennas and the interactions between the RC mode stirrers, biological loads, and intruding metallic infrastructures, this approach yields actionable data that can drive critical decisions at the study design stage or even clarify rodent exposure histories a posteriori. While this "digital twin" approach significantly improves upon idealized plane-wave models, providing a robust predictive framework prior to physical experimental validation, its inherent reliance on specific material property assumptions and the selected operating frequency are noteworthy parameters to consider.

The most important take-away is that complexity matters. The inclusion of RF cavity behaviors and realistic RC features revealed that exposure imbalances significantly exceed those predicted by idealized Rayleigh fading models. While simplified PW models provided necessary early estimates when computational resources were limited, they are insufficient for determining reliable uncertainty bounds in modern bioassay designs.

Ultimately, the proposed "digital twin" methodology provides a predictive tool for the a priori optimization of bioassay setups, allowing researchers to test and refine mitigation strategies, such as rotational cage dynamics, well ahead of committing to a physical design. Furthermore, it may significantly improve a posteriori interpretations of bioassay results by highlighting whether localized exposures and the resulting thermal loads might have acted upon biological endpoints as previously unaccounted confounders.

REFERENCES

[1] K. B. Jung, T. H. Kim, J. L. Kim, H. J. Doh, Y. C. Chung, J. H. Choi, and J. K. Pack, "Development and validation of reverberation-chamber type whole-body exposure system for mobile-phone frequency," *Electromagn. Biol. Med.*, vol. 27, no. 1, pp. 73–82, Mar. 2008.

[2] J. Shi, J. Chakarothai, J. Wang, K. Wake, S. Watanabe, and O. Fujiwara, "Quantification and verification of whole-body-average SARs in small animals exposed to electromagnetic fields inside reverberation chamber," *IEICE Trans. Commun.*, vol. E97.B, no. 10, pp. 2184–2191, Oct. 2014.

[3] C. Li, L. Yang, B. Lu, Y. Xie, and T. Wu, "A reverberation chamber for rodents' exposure to wideband radiofrequency electromagnetic fields with different small-scale fading distributions," *Electromagn. Biol. Med.*, vol. 35, no. 1, pp. 30–39, Jan. 2016.

[4] M. Capstick, S. Kuehn, V. Berdinas-Torres, Y. Gong, P. F. Wilson, J. M. Ladbury, G. Koepke, D. L. McCormick, J. Gauger, R. L. Melnick, and N. Kuster, "A radio frequency radiation reverberation chamber exposure system for rodents," *IEEE Trans. Electromagn. Compat.*, vol. 59, no. 4, pp. 1041–1052, Apr. 2017.

[5] S. Jeon, A.-K. Lee, J. Wang, J.-K. Pack, Y.-B. Kim, Y. H. Ahn, K. Imaida, and H.-D. Choi, "Field uniformity assessment of a reverberation chamber for a large-scale animal study," *IEEE Access*, vol. 9, pp. 146471–146477, 2021.

[6] *NTP Technical Report on the Toxicology and Carcinogenesis Studies in HSD: Sprague Dawley Rats Exposed to Whole-Body Radio Frequency Radiation at a Frequency (900 MHz) and Modulations (GSM and CDMA) Used By Cell Phones*, document NTP TR 595, National Toxicology Program, 2018.

[7] *NTP Technical Report on the Toxicology and Carcinogenesis Studies in B6C3F1/N Mice Exposed to Whole-Body Radio Frequency Radiation at a Frequency (1,900 MHz) and Modulations (GSM and CDMA) Used by Cell Phones*, document NTP TR 596, National Toxicology Program, 2018.

[8] J. C. West, C. F. Bunting, and V. Rajamani, "Accurate and efficient numerical simulation of the random environment within an ideal reverberation chamber," *IEEE Trans. Electromagn. Compat.*, vol. 54, no. 1, pp. 167–173, Feb. 2012.

[9] A. D. Francesco, V. De Santis, G. Bit-Babik, and A. Faraone, "An efficient plane-waves superposition method for improved spatial correlation in simulated reverberation chambers," *IEEE Access*, vol. 10, pp. 119641–119648, 2022.

[10] Y. Gong, M. H. Capstick, S. Kuehn, P. F. Wilson, J. M. Ladbury, G. Koepke, D. L. McCormick, R. L. Melnick, and N. Kuster, "Life-time dosimetric assessment for mice and rats exposed in reverberation chambers for the two-year NTP cancer bioassay study on cell phone radiation," *IEEE Trans. Electromagn. Compat.*, vol. 59, no. 6, pp. 1798–1808, Dec. 2017.

[11] S. Sandeep, A. F. Peterson, and J. Wiart, "Whole body SAR estimation of a rodent inside a reverberation chamber," *J. Electromagn. Waves Appl.*, vol. 39, no. 18, pp. 2426–2445, Dec. 2025.

[12] S. Jeon, W. Jang, A.-K. Lee, H.-D. Choi, J.-K. Pack, J. Wang, and D. Kim, "Distances between rats in reverberation chambers used for large-scale experiments," *J. Electromagn. Eng. Sci.*, vol. 21, no. 2, pp. 148–152, Apr. 2021.

[13] R. Ito, S. Jeon, J. Wang, A.-K. Lee, J.-K. Pack, H.-D. Choi, Y. H. Ahn, and K. Imaida, "Quantification of exposure level in a reverberation chamber for a large-scale animal study," *IEEE J. Microw.*, vol. 2, no. 3, pp. 522–532, Jul. 2022.

[14] V. De Santis, A. D. Francesco, K. R. Foster, G. Bit-Babik, and A. Faraone, "Monte–Carlo based numerical dosimetry in reverberation chamber exposure systems employed for in-vivo rodent bioassays," *IEEE Access*, vol. 11, pp. 22018–22033, 2023.

[15] J. Chakarothai, J. Wang, O. Fujiwara, K. Wake, and S. Watanabe, "Dosimetry of a reverberation chamber for whole-body exposure of small animals," *IEEE Trans. Microw. Theory Techn.*, vol. 61, no. 9, pp. 3435–3445, Sep. 2013.

[16] J. Chakarothai, J. Shi, J. Wang, O. Fujiwara, K. Wake, and S. Watanabe, "Numerical techniques for SAR assessment of small animals in reverberation chamber," *IEEE Electromagn. Compat. Mag.*, vol. 4, no. 1, pp. 57–66, Feb. 2015.

[17] A. Faraone, G. Bit-Babik, P. Russo, A. D. Leo, V. M. Primiani, and V. D. Santis, "Computational RF dosimetry of rodents cohorts in a realistic reverberation chambers at 900 MHz," in *Proc. Int. Symp. Electromagn. Compat.-EMC Eur.*, Bruges, Belgium, Sep. 2024, pp. 957–960.

[18] A. Faraone, G. Bit-Babik, K. Sanderson, P. Russo, A. D. Leo, V. Mariani Primiani, and V. D. Santis, "Numerical characterization of rodent exposure imbalances in large reverberation chambers," in *Proc. Int. Symp. Electromagn. Compat.-EMC Eur.*, Paris, France, Sep. 2025, pp. 1103–1107.

[19] D. Appicciutoli, G. Buoncompagni, and V. M. Primiani, "Experimental activity in using a reverberation chamber for emission and shielding effectiveness measurements: Comparison with traditional deterministic methods," in *Proc. EMC Eur., Int. Symp. Electromagn. Compat.*, Sep. 2004, pp. 1–6, doi: 10.23919/emc.2004.10805846.

[20] *Electromagnetic Compatibility (EMC)—Part 4-21: Testing and Measurement Techniques—Reverberation Chamber Test Methods*, IEC Standard 61000-4-21:2011, 2011.

[21] D. A. Hill, "Electromagnetic theory of reverberation chambers," U.S. Dept. Commerce, National Institute of Standards and Technology, Boulder, CO, NIST, Tech. Rep. 1506, Dec. 1998.

[22] F. Moglie and V. Mariani Primiani, "Numerical simulations of field values, wave impedance, and received power inside a nonideal reverberation chamber," *IEEE Trans. Electromagn. Compat.*, vol. 56, no. 4, pp. 994–997, Aug. 2014, doi: 10.1109/TEMC.2013.2290806.

ANTONIO FARAONE (Senior Member, IEEE) was born in Rome, Italy, in 1966. He received the Ph.D. degree in applied electromagnetics from the University of Rome "La Sapienza," Rome, in 1997. In 1997, he joined the Motorola (later Motorola Solutions) Corporate Electromagnetic Energy (EME) Research Laboratory, Fort Lauderdale, FL, USA, where he engaged in mobile antenna technology and RF dosimetry research and IEEE and IEC RF exposure safety and product compliance standards; he currently works as the Chief EME Scientist, overseeing product RF exposure compliance. He is also a Motorola Innovators Circle (MIC) Member, a Master Innovator, and a Dan Noble Fellow. He has co-authored about 40 refereed journal publications and holds 50 patents, mostly on RF and antenna technologies. He was a recipient of the IEC 1906 Award and serves as the Secretary for the Technical Committee 95 within the IEEE International Committee on Electromagnetic Safety (www.ices-emfsafety.org). Since 2018, he has been chairing the Board of Directors of the Mobile and Wireless Forum (www.mwfai.org), an international industry association supporting research into RF health and safety, and promoting wireless device integrity and accessibility.

GIORGI BIT-BABIK (Senior Member, IEEE) received the M.Sc. (Hons.) and Ph.D. degrees in radio physics and electronics from Tbilisi State University (TSU), Tbilisi, Georgia, in 1994 and 1998, respectively. He was a Research Staff Member and later an Associate Professor at TSU. In 2001, he joined the Electromagnetic Energy (EME) Research Laboratory, Motorola Inc., Fort Lauderdale, FL, USA. He is currently a Distinguished Member of the Technical Staff and Motorola Innovators Circle (MIC) Member at Motorola Solutions, Inc. He holds 33 patents mostly in antenna technology and published more than 90 journal and conference publications in applied electromagnetics and RF exposure dosimetry. His work is related to antenna technology research and development, RF exposure dosimetry, and compliance assessment and standards. He is actively involved in the IEEE ICES TC34 & TC95 and IEC TC106 standards committees developing measurement and numerical methods for RF exposure assessment. He is a member of multiple working groups and project teams within ICES TC34 and TC106 and a Convenor of the JWG IEC/IEEE 62704-2. He serves as a Technical Advisor for the USNC TAG106. He was a recipient of the IEC 1906 Award and the IEEE Standards Association International Award.

KEVIN SANDERSON received the Bachelor of Science degree in physics with minors in electrical engineering and computer science from the University of Illinois Urbana–Champaign. He is planning to pursue the M.S. degree. He has experience in RF engineering and electromagnetic simulation through his internships at Motorola Solutions, Fort Lauderdale, FL, USA, focusing on antenna design and RF circuit optimization. His work includes contributions to conference publications and a pending patent. His research interests include connecting physics with practical applications in computing and electrical systems.

PAOLA RUSSO (Senior Member, IEEE) received the Ph.D. degree in electronic engineering from the Polytechnic University of Bari, Bari, Italy, in April 1999. From January 2005 to July 2019, she was an Assistant Professor with the Polytechnic University of Marche (UnivPM), Ancona, Italy, where she was appointed as an Associate Professor, in August 2020. She teaches antenna design and fundamental of electromagnetics. Her main research interests include the application of numerical modeling to EMC problems, antenna problems, plasma antennas, and electromagnetic sensors. She is a member of Italian Electromagnetic Society (SIEm) and the Scientific Board of Italian Center for the study of the interactions between Electromagnetic Fields and Biosystem (ICEmB).

ALFREDO DE LEO (Senior Member, IEEE) was born in Bari, Italy, in 1975. He received the Graduate degree (summa cum laude) in electronic engineering and the Ph.D. degree in electromagnetism and bioengineering from the Università Politecnica delle Marche, Italy, in 1999 and 2014, respectively. He is currently with the Università Politecnica delle Marche, where he teaches ''industrial application of electromagnetic fields'' and ''electrical systems for renewable energy.'' His current research interests include the development of electromagnetic models, laboratory experiments, numerical simulation techniques related to interactions between electromagnetic fields and biological beings, and remote sensing of physiological activities and reverberation chambers. He is a member of the IEEE Electromagnetic Compatibility Society, Italian Society of Electromagnetics (SIEM), and Consorzio Nazionale Interuniversitario per le Telecomunicazioni (CNIT). He is an Expert Member of IET TC 77/JMT MU Technical Committee No. 77: Electromagnetic Compatibility JMT MU: Measurement Uncertainty and CEI Technical Subcommittees SC210/7713 and SC 210/A.

VALTER MARIANI PRIMIANI (Senior Member, IEEE) received the Laurea degree (summa cum laude) in electronic engineering from the University of Ancona, Ancona, Italy, in 1990.

He is currently a Full Professor in electromagnetic compatibility (EMC) with the Università Politecnica delle Marche, Ancona. He is also a member of the Department of Information Engineering, where he is also responsible for the EMC Laboratory. His research interests include the prediction of digital printed circuit board radiation, the radiation from apertures, the electrostatic discharge coupling effects modeling, and the analysis of emission and immunity test methods. Since 2003, he has been also involved in research activities on the application of reverberation chambers for compliance testing, metrology applications and multipath propagation emulation. He has been a member of the COST Action 1407 ACCREDIT on the characterization of stochastic emissions from digital equipment. He is a Senior Member of the IEEE (EMC Society) and a member of Italian Society of Electromagnetics. Since 2007, he has been or was an active member of some Working Groups for the development of IEEE Standards: 299.1, 1302, 2715, and 2716 on shielding effectiveness measurements. Since 2014, he has also been a member of the International Steering Committee of EMC Europe. Since 2017, he has also been the Chair of the working group for the IEEE Standard 2718 for the characterization of stochastic emissions. He was involved in European project RISE-6G on the using of Reconfigurable Intelligent Sustainable Environments for 6G Wireless Networks. He is currently involved in the Doctoral Network MSCA 2022 ''NEPIT'' as responsible for Ancona Unit. He is also an Italian Member of the Joint Task Force CISPR/A/SC77B on Reverberation chambers. He is also an Associate Editor of the journal *IET Science, Measurement & Technology*.

VALERIO DE SANTIS (Senior Member, IEEE) received the Laurea degree (summa cum laude) in telecommunication engineering and the Ph.D. degree in electrical and computer engineering from the University of L'Aquila, L'Aquila, Italy, in 2006 and 2010, respectively.

He joined the Foundation for Research on Information Technologies in Society, IT'IS Foundation, Switzerland, from 2011 to 2013, holding the position of the Project Leader. He was an Assistant Professor with Nagoya Institute of Technology, Nagoya, Japan, from January to March 2015. He is currently an Associate Professor at the University of L'Aquila. His current research interests include wireless power transfer, numerical methods and techniques, electromagnetic compatibility (EMC), bioelectromagnetics, and human exposure safety, all testified by more than 100 papers published in peer-reviewed journals and conferences.

Prof. De Santis is participating in and leading several standardization efforts in the human exposure and product safety domain. He is a member of the BioElectroMagnetic (BioEM) Society, of the IEC TC 106, and was the Secretary of IEEE ICES TC95 SC6. He received the Second-Best Student Paper Award at the BioEM Annual Meeting, Cancun, Mexico, in 2006, the Best Student Paper Award at the IEEE International Symposium on EMC, Honolulu, USA, in 2007, the Best Poster Award at the IEEE Biennial Conference on Electromagnetic Field Computation (CEFC), Hangzhou, China, in 2018, and the 2025 Motohisa Kanda Award for the most cited paper of IEEE Transactions on Electromagnetic Compatibility in the past five years.